Erosion wear at the bend of pipe during tailings slurry transportation: Numerical study considering inlet velocity, particle size and bend angle

Qiusong Chen, Hailong Zhou, Yunmin Wang, Daolin Wang, Qinli Zhang, and Yikai Liu

Articles you may be interested in

Chellaganesh Duraipandi, Adam Khan M, Winowlin Jappes J. T., Nouby M. Ghazaly, and Peter Madindwa Mashinini, Solid particle erosion studies of thermally deposited alumina–titania coatings on an aluminum alloy, *Int. J. Miner. Metall. Mater.*, 28(2021), No. 7, pp. 1186-1193. https://doi.org/10.1007/s12613-020-2099-8

Mehmet Akif Erden and Fatih Aydın, Wear and mechanical properties of carburized AISI 8620 steel produced by powder metallurgy, *Int. J. Miner. Metall. Mater.*, 28(2021), No. 3, pp. 430-439. https://doi.org/10.1007/s12613-020-2046-8

Alexander M. Klyushnikov, Rosa I. Gulyaeva, Evgeniy N. Selivanov, and Sergey M. Pikalov, Kinetics and mechanism of oxidation for nickel-containing pyrrhotite tailings, *Int. J. Miner. Metall. Mater.*, 28(2021), No. 9, pp. 1469-1477. https://doi.org/10.1007/s12613-020-2109-x

Navid Mehdipour, Milad Rezaei, and Zeynab Mahidashti, Influence of glycine additive on corrosion and wear performance of electroplated trivalent chromium coating, *Int. J. Miner. Metall. Mater.*, 27(2020), No. 4, pp. 544-554. https://doi.org/10.1007/s12613-020-1975-6

Dao-ying Chen, Ying Liu, Ren-quan Wang, and Jin-wen Ye, Sliding wear behaviour of Fe/316L/430–Ti(C,N) composites prepared via spark plasma sintering and subsequent heat treatment, *Int. J. Miner. Metall. Mater.*, 28(2021), No. 7, pp. 1215-1223. https://doi.org/10.1007/s12613-020-2108-y

Hong-mei Zhang, Yan Li, Ling Yan, Fang-fang Ai, Yang-yang Zhu, and Zheng-yi Jiang, Effect of large load on the wear and corrosion behavior of high-strength EH47 hull steel in 3.5wt% NaCl solution with sand, *Int. J. Miner. Metall. Mater.*, 27(2020), No. 11, pp. 1525-1535. https://doi.org/10.1007/s12613-020-1978-3

IJMMM WeChat   QQ author group

Erosion wear at the bend of pipe during tailings slurry transportation: Numerical study considering inlet velocity, particle size and bend angle

Qiusong Chen[1,2], *Hailong Zhou*[1], *Yunmin Wang*[1,2], *Daolin Wang*[1],✉, *Qinli Zhang*[1], *and Yikai Liu*[3]

1) School of Resources and Safety Engineering, Central South University, Changsha 410083, China
2) Sinosteel Maanshan General Institute of Mining Research Co., Ltd., Maanshan 243000, China
3) Department of Geosciences, University of Padova, 35131 Padova, Italy

Abstract: Pipeline hydraulic transport is a highly efficient and low energy-consumption method for transporting solids and is commonly used for tailing slurry transport in the mining industry. Erosion wear (EW) remains the main cause of failure in tailings slurry pipeline systems, particularly at bends. EW is a complex phenomenon influenced by numerous factors, but research in this area has been limited. This study performs numerical simulations of slurry transport at the bend by combining computational fluid dynamics and fluid particle tracking using a wear model. Based on the validation of the feasibility of the model, this work focuses on the effects of coupled inlet velocity (IV) ranging from 1.5 to 3.0 m·s⁻¹, particle size (PS) ranging from 50 to 650 μm, and bend angle (BA) ranging from 45° to 90° on EW at the bend in terms of particle kinetic energy and incidence angle. The results show that the maximum EW rate of the slurry at the bend increases exponentially with IV and PS and first increases and then decreases with the increase in BA with the inflection point at 60° within these parameter ranges. Further comprehensive analysis reveals that the sensitivity level of the three factors to the maximum EW rate is PS > IV > BA, and when IV is 3.0 m/s, PS is 650 μm, and BA is 60°, the bend EW is the most severe, and the maximum EW rate is 5.68×10^{-6} kg·m⁻²·s⁻¹. In addition, When PS is below or equal to 450 μm, the maximum EW position is mainly at the outlet of the bend. When PS is greater than 450 μm, the maximum EW position shifts toward the center of the bend with the increase in BA. Therefore, EW at the bend can be reduced in practice by reducing IV as much as possible and using small particles.

Keywords: tailings transportation; erosion wear; pipe wear; CFD; numerical simulation.

1. Introduction

From circulatory and respiratory systems to chemical and plumbing networks, a good understanding of hydraulic flows is essential in many natural settings and engineering applications [1–3]. Even modest variations in hydraulic flow properties could bring significant economic and environmental benefits to real field trials, for example, improving the quality of overall pipeline systems [2], mitigating the gradual degradation of constructions [4], and minimizing the required power capacity of turbines [5]. Especially in the modern mining industry, the overall efficiency and reliability are modulated for a reliable and advanced hydraulic pumping system design [2,6]. From the transport and storage of the excavated ore resources to the concentration and pumping of backfill materials for goaf management, a large suite of equipment is exposed to hydraulic flows, including pipelines, pumps, and valves, and will be damaged or even ruptured by erosion wear (EW) in varying degrees, representing a grand challenge in the sustainability and profitability of the mining industry [7–11].

The factors affecting pipeline damage are mainly derived from the origins of pipeline design, such as geometry parameters (pipe diameter and wall thickness), construction materials [1,12], and the nature of the pumped paste, including the physical properties of the solid particles, viscosity and components of the slurry, and unsteady or pulsatile flow conditions [13–15]. Among all the attributed components of a conveying system, bends (elbows and sweeps) are the most potentially problematic and severely affected by EW [16]. The most straightforward solution for minimizing the EW of vessels and pipes network is through relatively unsophisticated geometry map design; however, due to the inherent limitations (for instance, the spatial and space restrictions) in field trials, bend sections are inevitably and extensively used [5]. Therefore, broad concerns are beginning to uncover the influence of relevant factors on the damage of bends to ensure the safe, efficient, and stable operation of the entire conveying system.

Many longstanding scientific and engineering difficulties remain in revealing this multifactor controlled dynamic erosion–corrosion behavior under critical transportation conditions. Only a few experiments have been performed probing the properties of the slurry impact directly responsible for

---

EW failure [17–19]. With the rapid development of computer science and modern numerical techniques, numerical simulations for low cost and controllability can extend deep insights into pipeline wear studies [20]. Tan *et al.* [21–22] combined computational fluid dynamics (CFD) and discrete element method (DEM) to study the solid–fluid multiphase flow problem during concrete pumping and proposed a new time-averaged impact force-based collision strength model. The effects of slurry velocity, bending direction, and elbow angle on bend wear were also investigated, but bend erosion was only characterized through particle wall interaction forces rather than a wear model. Wu *et al.* [23] investigated the effect of high viscosity coal gangue slurry on pipe wear by combining the finite element method (FEM) and concluded that the erosion of the pipe wall by 15–30 mm particles is mainly caused by flow impact and tangential forces; however, the influencing factors on wear were not explored in depth. Kannojiya *et al.* [24] used ANSYS CFX software to investigate the erosion rate of particles at different slurry velocities and concentrations. Wang *et al.* [25] used CFD techniques to model and analyze the slurry flow and wall impact information to investigate the effects of particle concentration, length of straight pipe upstream between elbows, and inlet conditions on erosion behavior. Zhou *et al.* [26] used a CFD–DEM model to investigate the effect of coarse-grained slurry of 3.5 mm on pipe damage at different velocities and flow regimes. Although some of the factors influencing pipeline wear have been widely studied, most researchers have focused on the oil and gas industry [27–33]. Our understanding of EW in slurry pipes is still rudimentary and insufficient. Although recent progress allows us to understand the potential mechanism, current works primarily consider the effects in view of single factor models, which cannot go beyond and comprehensively reveal multiple interactions.

This work combines CFD, fluid particle tracking (FPT), and wear models to investigate the effects of three factors, inlet velocity (IV), particle size (PS), and bend angle (BA), on the maximum EW rate and location at the bend in slurry transportation. The contribution of this study lies in the comprehensive analysis of the individual effects of IV, PS, and BA on the EW rate and location at the bend and in the exploration of their combined effects and the development of an EW rate calculation model. The results provide an important basis for the design of the pipeline transportation system, which is of great significance for optimizing the performance of the pipeline by determining reasonable parameters that can help reduce the EW of the pipeline and ensure its stability and safety.

2. Model description

Considering that tailings slurry is a two-phase mixture of solid and liquid, this study uses a turbulence model to describe the flow behavior of the liquid phase, an FPT model to describe the slip behavior of solid particles, and an

erosion–corrosion research center (E/CRC) model to calculate the EW of the bend pipe wall. The specific models and equations are described as follows:

2.1. Turbulence model

The k–ε turbulence model is widely used in industrial applications and has been extensively employed in previous studies to describe the flow behavior of tailings slurry in pipeline transportation, where the slurry is considered an incompressible fluid [34–35]. In the current work, the k–ε turbulence model includes a continuity equation representing mass conservation and a momentum conservation equation. In addition, the model introduces two additional transport equations and two dependent variables: turbulent kinetic energy, k, and turbulent dissipation rate, ε.

The continuity equation for this model can be written as

$$\frac{\partial \rho}{\partial t} + \nabla \cdot (\rho \boldsymbol{u}) = 0 \tag{1}$$

The model momentum equation can be written as

$$\rho \frac{\partial \boldsymbol{u}}{\partial t} + \rho (\boldsymbol{u} \cdot \nabla) \boldsymbol{u} = \nabla \cdot (-p\boldsymbol{I} + \boldsymbol{K}) + \boldsymbol{F} + (\rho - \rho_{\text{ref}}) \boldsymbol{g} \tag{2}$$

where $\boldsymbol{K}$ is

$$\boldsymbol{K} = (\mu + \mu_{\text{T}}) \left(\nabla \boldsymbol{u} + (\nabla \boldsymbol{u})^{\text{T}} \right) \tag{3}$$

The transport equation for k is

$$\rho \frac{\partial k}{\partial t} + \rho \boldsymbol{u} \cdot \nabla k = \nabla \cdot \left[\left(\mu + \frac{\mu_{\text{T}}}{\sigma_k} \right) \nabla k \right] + P_k - \rho \varepsilon \tag{4}$$

where the production term P_k is

$$P_k = \mu_{\text{T}} \left[\nabla \boldsymbol{u} : \left(\nabla \boldsymbol{u} + (\nabla \boldsymbol{u})^{\text{T}} \right) - \frac{2}{3} (\nabla \cdot \boldsymbol{u})^2 \right] - \frac{2}{3} \rho k \nabla \cdot \boldsymbol{u} \tag{5}$$

The transport equation for ε is

$$\rho \frac{\partial \varepsilon}{\partial t} + \rho \boldsymbol{u} \cdot \nabla \varepsilon = \nabla \cdot \left[\left(\mu + \frac{\mu_{\text{T}}}{\sigma_\varepsilon} \right) \nabla \varepsilon \right] + C_{\varepsilon 1} \frac{\varepsilon}{k} P_k - C_{\varepsilon 2} \rho \frac{\varepsilon^2}{k} \tag{6}$$

where ρ is the density (kg·m^{-3}), $\boldsymbol{u}$ is the velocity vector (kg·m^{-3}), $\boldsymbol{I}$ is the identity matrix (unitless), $\boldsymbol{K}$ is the viscous stress tensor (Pa), $\boldsymbol{F}$ is the volume force vector (N·m^{-3}), ρ_{ref} is the reference density (kg·m^{-3}), $\boldsymbol{g}$ is the acceleration of gravity (m·s^{-2}), μ is the dynamic viscosity (Pa·s), and μ_{T} is the turbulent viscosity (Pa·s). Bold fonts in the equations represent vectors. The closure factors used in Eqs. (4) and (6) are shown in Table 1.

Table 1.   Closure factors

σ_k	σ_ε	$C_{\varepsilon 1}$	$C_{\varepsilon 2}$
1.0	1.3	1.92	1.44

2.2. FPT model

The FPT model is designed to describe the dynamic behavior of microscopic and macroscopic particles in fluids based on Newton's second law in COMSOL Multiphysics software [36–37]. The particle equations of motion can be written as

1610

Int. J. Miner. Metall. Mater., Vol. 30, No. 8, Aug. 2023

$$\frac{\mathrm{d}}{\mathrm{d}t}\left(m_{\mathrm{p}}v\right) = F_{\mathrm{D}} + F_{\mathrm{g}} + F_{\mathrm{ext}} \tag{7}$$

where v and F_{D} are as follows:

$$v = \frac{\mathrm{d}q}{\mathrm{d}t} \tag{8}$$

$$F_D = \left(\frac{1}{\tau_{\mathrm{p}}}\right)m_{\mathrm{p}}(u - v) \tag{9}$$

where τ_{p} is

$$\tau_{\mathrm{p}} = \frac{\rho_{\mathrm{p}}d_{\mathrm{p}}^2}{18\mu} \tag{10}$$

where m_{p} is the particle mass (kg), v is the particle velocity (m·s^{-1}), and F_{D}, F_{g}, and F_{ext} are the drag, gravity, and other forces, respectively (N). τ_{p} is the particle velocity response time (s), u is the fluid velocity at the particle's position (m·s^{-1}), ρ_{p} is the particle density (kg·m^{-3}), and d_{p} is the particle diameter (m).

2.3. Wear model

On the basis of the above k–ε turbulence and FPT models derived from each CFD cell recording the collision information of the impacting particles close to the pipe wall, an accurate E/CRC pipe wear model case is introduced to predict the EW of the pipe wall by the slurry [38]. The E/CRC model defines the erosion rate in terms of the ratio of mass lost by the surface to the mass of incident particles:

$$\mathrm{ER} = CF_{\mathrm{s}}(\mathrm{BH})^{-0.59}(v)^n F(\alpha) \tag{11}$$

where ER is the erosion rate (kg·m^{-2}·s^{-1}), C is an erosion model coefficient, F_{s} is the particle shape coefficient, BH is the Brinell hardness of the wall material (dimensionless), v is particle velocity (dimensionless), n is an empirical constant equal to 2.41, and $F(\alpha)$ is the impact angle function defined as follows:

$$F(\alpha) = 5.40\alpha - 10.11\alpha^2 + 10.93\alpha^3 - 6.33\alpha^4 + 1.42\alpha^5 \tag{12}$$

where α is the angle of particle incidence.

2.4. Simulation scenario and boundary conditions

For improved computational efficiency, an L-shaped pipeline is constructed with geometric parameters based on actual mining conditions. Fig. 1 shows the simulated geometric model of a 0.12 m diameter (D) pipe, which consists of a vertical pipe ($15D$ in length) and a bend (0.38 m inner radius of the bend) connected to a horizontal pipe ($30D$ in length). The effect of PS, IV, and BA on the EW of the bend is considered in this work, with four levels of each factor selected to combine with each other to form 64 simulation scenarios. The PSs are set to 50, 250, 450, and 650 µm, the IVs are set to 1.5, 2.0, 2.5, and 3.0 m·s^{-1}, and the BAs are set to 45°, 60°, 75°, and 90°. Water is chosen as the particle carrier, and the iron pipe material is selected with a particle count of 6×10^4 per release. The relevant parameters for the simulation are shown in Table 2. In addition, the geometry is meshed as a structured network. Although different BAs lead to different numbers of meshes, the structure of the meshing shows no difference and consists of prisms and tetrahedra. The average unit mass of the mesh is 0.73, indicating good division.
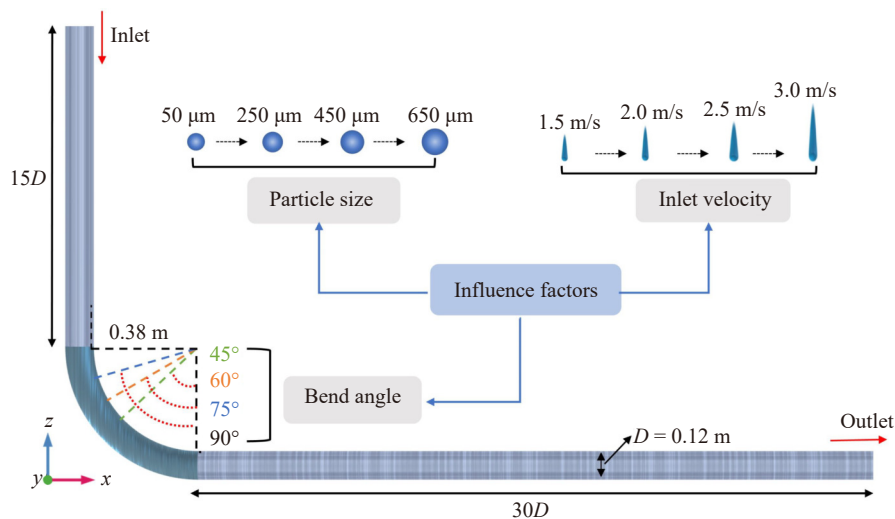

Fig. 1.   Modeling set-up and definition of variables.

The boundary conditions for the turbulent k–ε model are set to the velocity inlet, pressure outlet (with a value of 0 relative to the inlet), no slip on the walls. And the fluid is considered incompressible. The FPT model is set to the inlet (based on turbulence model velocity inlet), pipe wall (adhesion), and outlet wall (disappearance) conditions. The whole model is subjected to gravity in the negative direction of the z-axis ($g = 9.8$ m·s^{-2}), and the effect of temperature is not considered.

3. Results and discussion

3.1. Model validation

To probe the granular dynamics associated with near-

Table 2.　Simulation parameters

Parameter	Value
Density of the liquid / (kg·m^{-3})	1000
Liquid viscosity / (Pa·s)	0.001
Temperature / K	293.15
Reference pressure level / Pa	101325
Particle density / (kg·m^{-3})	2665
Density of the pipe material iron / (kg·m^{-3})	7860
Erosion model coefficient	2.17×10^{-7}
Particle shape coefficient	0.2
Brinell hardness of the wall	200

threshold mixture transport in real annular tube trials, we used a published dataset [39] to validate the proposed model. The EW tests in Zeng *et al.*'s work were conducted with a temperature of 60°C and a flow rate of 4 m·s^{-1} in 50 mm X65 carbon steel (Table S1). The particles were sand with a density of 2650 kg·m^{-3}, a mass flow rate of 235 g·s^{-1}, and PS in the range of 400–500 μm, which was taken as the average PS of 450 μm in the current work. Fig. 2 shows the results of the simulation data compared with the experimental data. Both EW rates increase gradually from the inlet to the outlet of the bend. Compared with the simulation data, the experimentally measured EW rate is significantly higher at the bend inlet probably because some particles with a PS greater than 450 μm are less affected by fluid traction in the actual transport system and can maintain their original direction of flow, resulting in great EW by collision with the area around the bend inlet. The simulation and experimental data are generally in excellent agreement, indicating that the numerical model is suitable for bend EW studies.
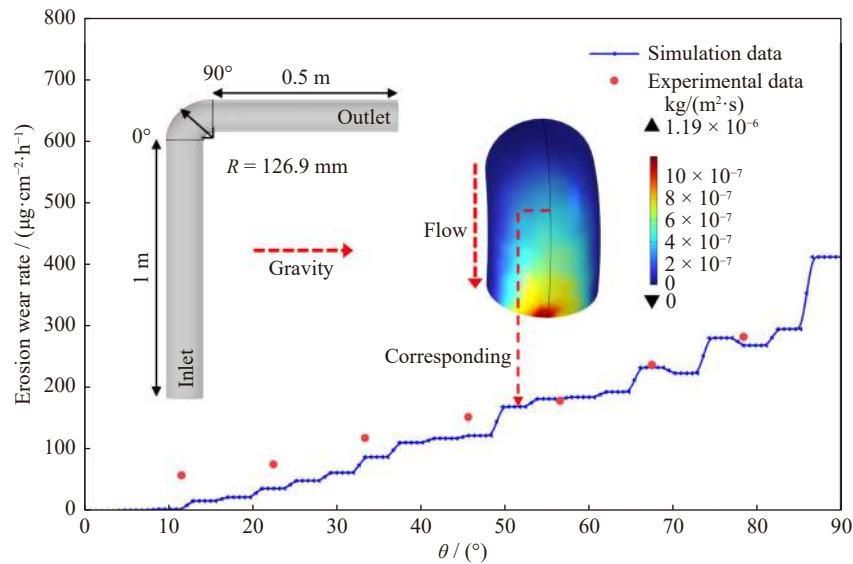

Fig. 2.　Comparison of simulation results with the experimental dataset proposed by Zeng *et al.* [39].

3.2. Effect of inlet velocity on erosion wear

Fig. 3 shows the EW curves of the simulated scenarios for IV ranging from 1.5 to 3 m/s, with BA and PS equivalent to 90° and 450 μm, respectively. The proposed bend is intercepted along with a 0.25 m section of the horizontal pipe, in consideration that the horizontal pipeline section connected to the outlet of the bend might also be subjected to EW (Fig. 3(a)). Simulation results showed that the maximum EW rate increases exponentially at the bend with the increasing IV. For example, the maximum EW rate of the slurry increases from 4.13×10^{-8} to 2.09×10^{-6} kg·m^{-2}·s^{-1} at the bend as the IV increases from 1.5 to 3.0 m·s^{-1}, a difference of two orders of magnitude (Fig. 3(b)). Moreover, the angular position of the maximum EW ranges from 84° to 90° at different IVs, indicating that the area of maximum EW concentration is mainly at the bend outlet. The specific EW distribution is shown in Fig. 3(c).

As the significant drivers point to the EW rate kinetic energy and incidence angle manipulation will simultaneously alter the pipeline status [40]. The EW degree of rigid materi-

als (e.g., iron and steel) in the small angles increases with increasing slurry incidence angle (the angle between the tangential direction of the pipe surface and the incidence trajectory) and particle kinetic energy [41]. Owing to different definitions, the incidence angle is the angle between the direction normal to the surface of the pipe and the incidence trajectory in this work, and both are complementary to each other. Therefore, the smaller the incidence angle, the higher the degree of EW in the range of 0°–60°.

In the individual investigation of these variables, the collision of particles onto the pipe surface moves toward the horizontal sections due to the increased IV values, with the maximum kinetic energy increasing from 1.18×10^{-7} to 6.08×10^{-7} J (Fig. 4(a)). This collision shift could be partially explained by the combined effects of fluid drag, gravity, and centrifugal force at the bend; the increase in IV leads to the great initial kinetic energy of the particles and the relative weakening of the fluid layer's ability to bind the particles, which increases the particles' capability of maintaining their original direction of motion and the chance of colliding with
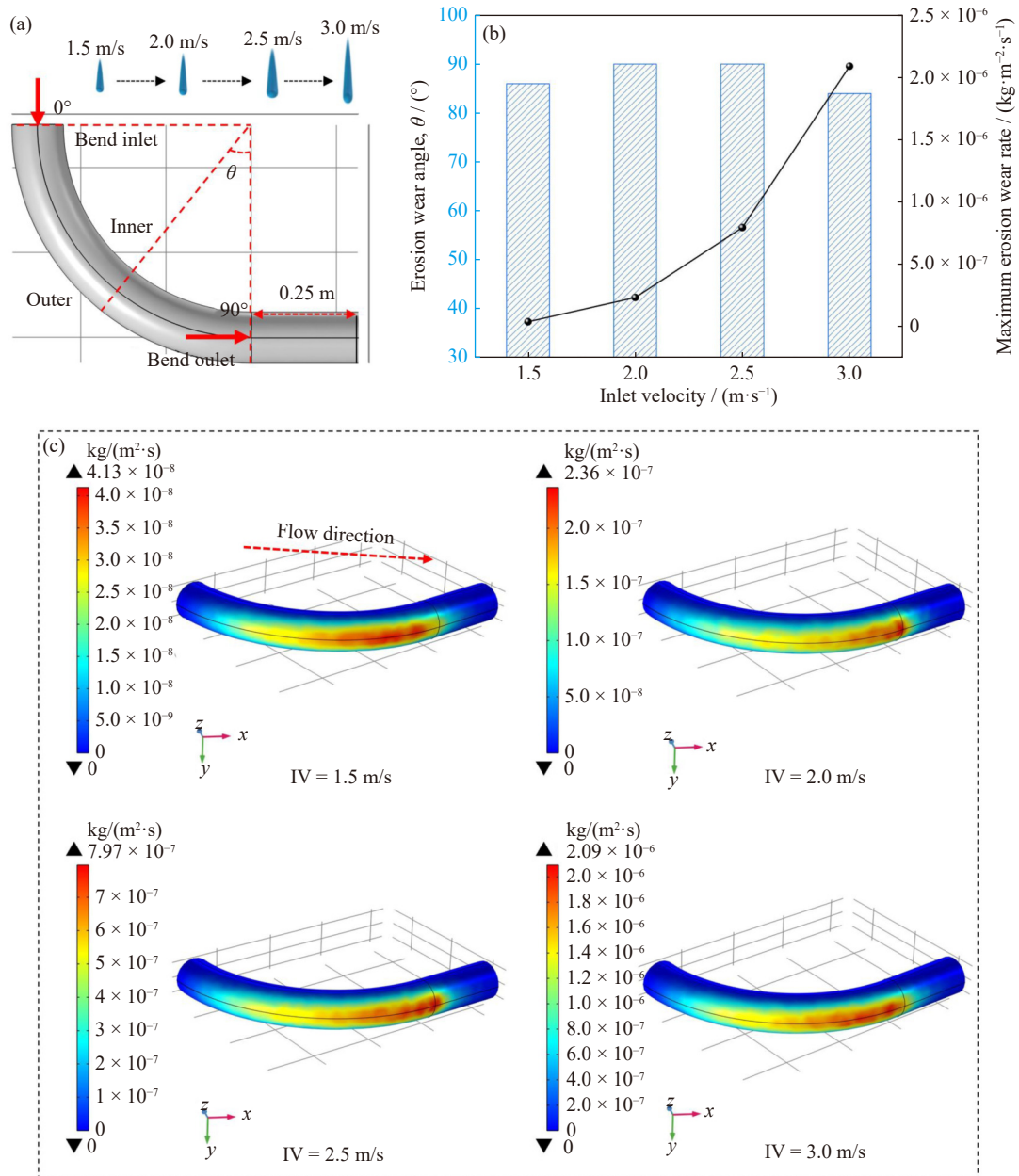
Fig. 3. Slurry transport at the bend with different inlet velocities (bend angle of 90° and particle size of 450 μm): (a) intercepted geometric pipe (*θ* refers to the angle used to illustrate the position of the maximum erosion wear, corresponding to (b)), (b) maximum erosion wear rate and corresponding position, and (c) distribution of bend erosion wear rate at the bend.

the outer pipe wall. In addition, the high kinetic energy values induce a small incidence angle and a strong shearing and collision effect on the pipe wall (Fig. 4(b)), resulting in severe EW.

For the angular position of the maximum EW, the angle of incidence at the bend outlet for different IVs is small, and the kinetic energy of the particles is high, so the maximum EW is mainly concentrated at the bend outlet. In addition, the collision of particles with the outer of the pipe is observed at the horizontal pipe, which is different from the V-shaped EW that occurs only at the bend of the pneumatic conveying particles [42–43]. The trailing force of the fluid is more restrictive to the particles than to gas, which changes the direction of particle movement to a certain extent.

3.3. Effect of particle size on erosion wear

A model was constructed using four different insert flows with the mean PS values ranging from 50 to 650 μm to reveal the role of PS in pipeline erosion. Fig. 5(a) shows the graphical structure of the bend simulation, which consists of an intercepted bend along with a 0.25 m horizontal pipe section. Fig. 5(b) displays the maximum EW rate and the corresponding angular position for different PS values at the bend (BA = 60°, IV = 1.5 m/s). The results suggested that the maximum EW rate at the bend increases exponentially with the increase in PS, with the maximum EW rate (2.28×10^{-7} kg·m^{-2}·s^{-1}) found at PS of 650 μm and the lowest EW rate (8.25×10^{-11} kg·m^{-2}·s^{-1}) at PS of 50 μm (Fig. 5(b)). Especially at the horizontal section, the stream with a PS value of
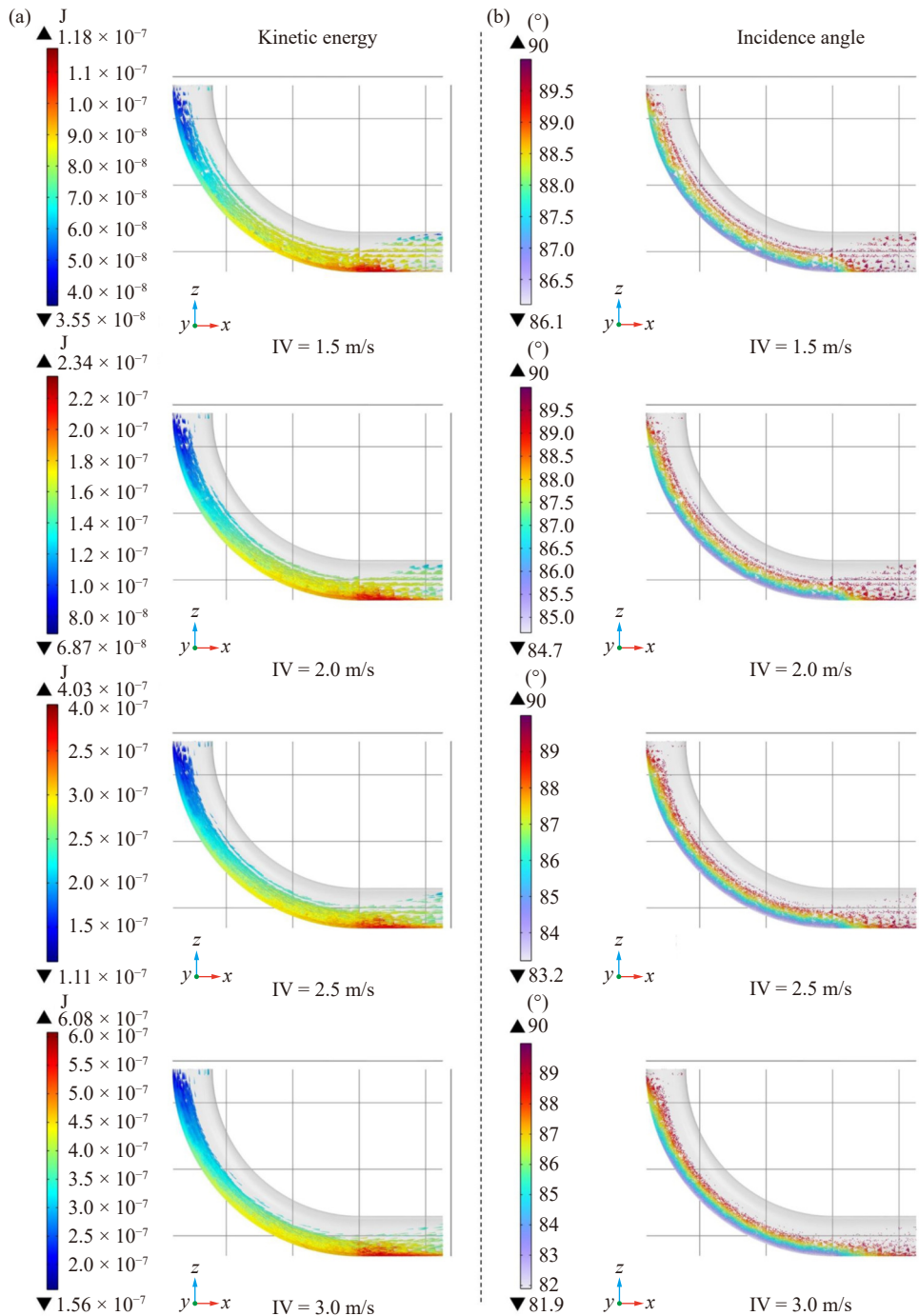
Fig. 4. Slurry transport at the bend with different inlet velocities (bend angle of 90° and particle size of 450 μm): (a) particle kinetic energy and (b) particle incidence angle.

50 μm has relatively less severe EW on the pipe wall, and only slight wear occurs at the outlet of the bend (Fig. 5(c)). The corresponding erosion angles are approximately at 89° (Fig. 5(b) and (c)), which is consistent with the findings in the experimental work of Blanchard *et al.* [44]. The erosion angles presented in the elbow are almost identical for different PS values applied in the loop systems, further indicating the reliability of the numerical model.

By contrast, the incident angle of the particles at the bend becomes smaller with the increase in PS values, with most of the erosion of the particles transferred from parallel friction

to angled shearing (Fig. 6). Such modification of particle movement accelerates the particle wall collision frequency and thereby remarkably increases the erosion to the bend wall. The estimated kinetic energy and incidence angle values are given in Fig. 6(a) and (b). The number of particles colliding with the pipe wall increases with the increase in PS value. and gradually moves toward the outer side of the pipe, possibly due to the low kinetic energy values of the small-sized particles that hit the pipe wall at a low frequency. In addition, the fluid with large particles shows a high kinetic energy value (Fig. 6(a)), with the simulated kinetic energy in-
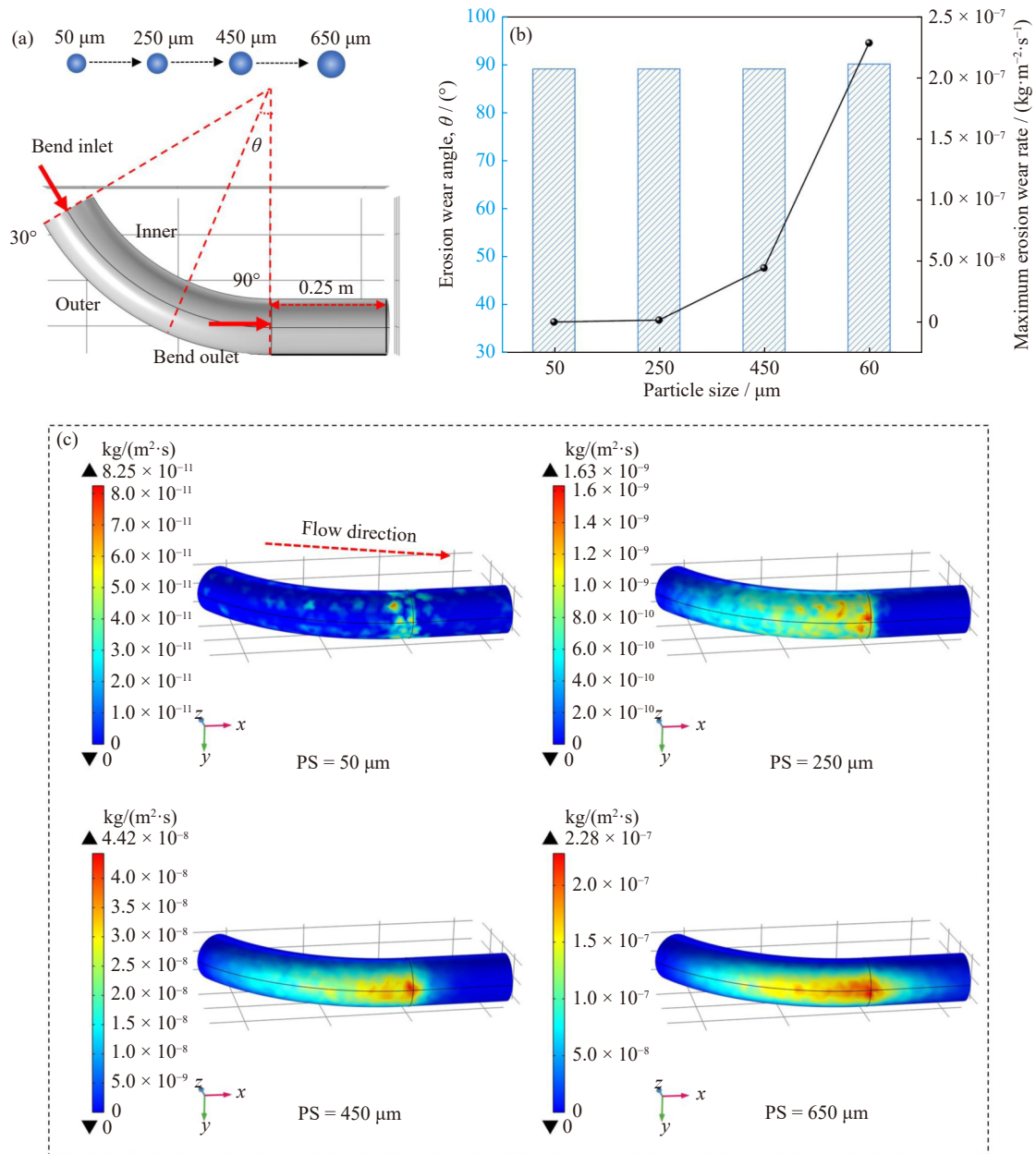
Fig. 5.   Slurry transport at the bend with different particle sizes (bend angle of 60° and inlet velocity of 1.5 m/s): (a) intercepted geometric pipe, (b) maximum erosion wear rate and corresponding position, and (c) distribution of bend erosion wear rate at the bend.

creasing from 1.10×10^{-10} J at PS of 50 μm to 4.21×10^{-7} J at PS of 650 μm. The particle flow characteristics at the bend area are mainly influenced by aerodynamic and centrifugal forces, suggesting that the stream with small particles tends to demonstrate small forces and lower the kinetic energy values and frequency of collision. With the increase in PS, the particles may interfere with the relatively constant fluid layers, resulting in a collision concentration close to the bend outlet area (Fig. 6(b)).

3.4. Effect of bend angles on erosion wear

As shown in Fig. 7(a), bends with angles of 45°, 60°, 75°, and 90° were applied to investigate the effect of EW on the surface of the pipe. Fig. 7(b) shows the maximum EW rate and the corresponding erosion position at the bend (with a constant PS value of 650 μm and IV of 2.5 m·s⁻¹) with respect to different BA values. The position of maximum EW is initially raised at the bend outlet and then gradually shifts toward the center. This position shift is highly pronounced at high BA values. As the BA increases from 45° to 60°, the EW angles are illustrated approximately at the same position (89° and 90°, respectively). When the BAs are 75° and 90°, the EW angles move to 77° and 62°, respectively (Fig. 7(b)). In addition, the estimated maximum EW rates slightly increase (from 2.23×10^{-6} to 2.55×10^{-6} kg·m⁻²·s⁻¹) with the BA increasing from 45° to 60°. The EW rate decreases to 2.41×10^{-6} kg·m⁻²·s⁻¹ as the BA increases to 90°. The overall EW rate difference is only 0.32×10^{-6} kg·m⁻²·s⁻¹, which indicates the slightly weaker effect of the BA gradient change on the maximum EW rate at the bend compared with the IV

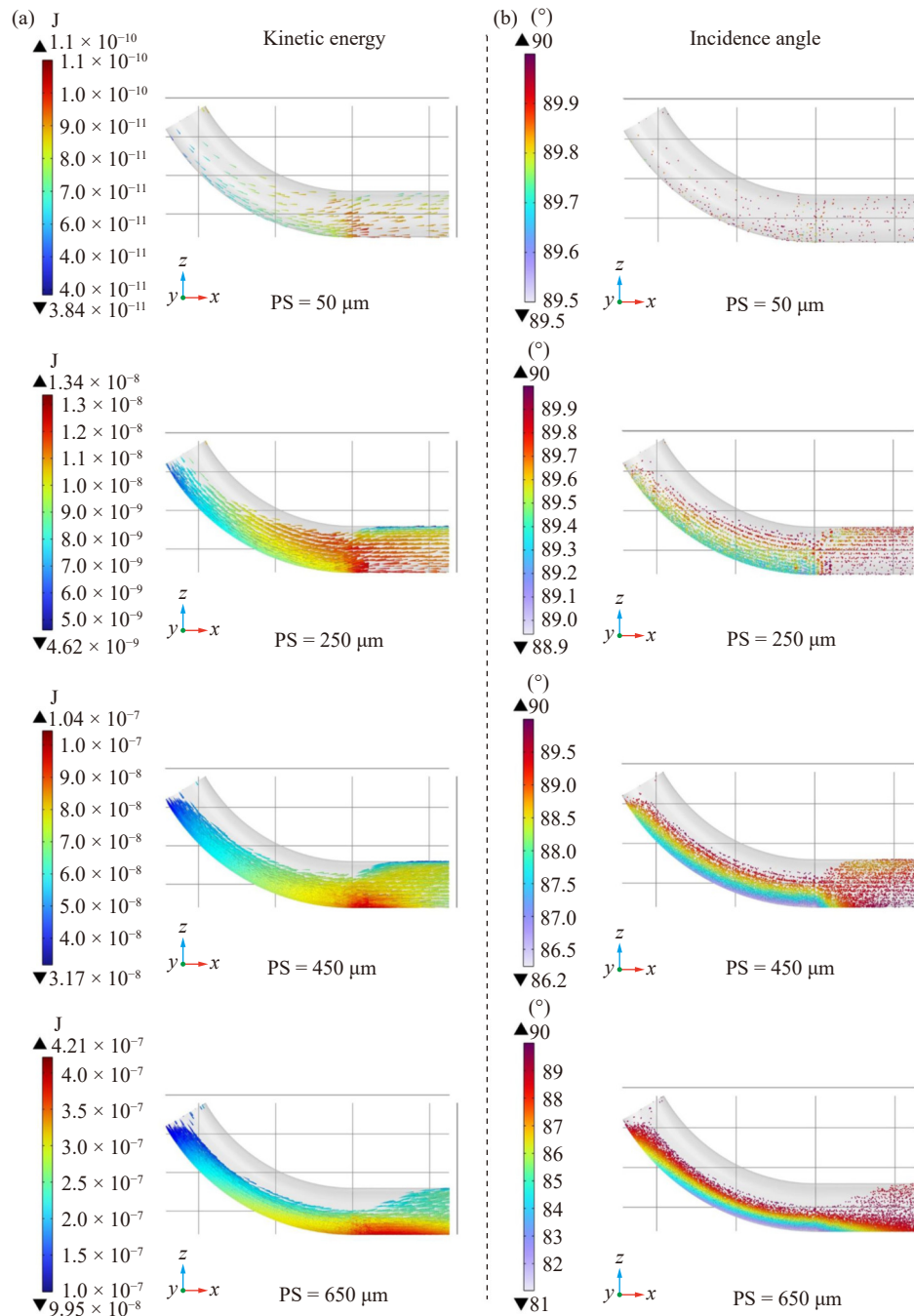**Fig. 6.** Slurry transport at the bend with different particle sizes (bend angle of 60° and inlet velocity of 1.5 m·s^{-1}): (a) particle kinetic energy and (b) particle incidence angle.

and PS factors.

Fig. 8(a) and (b) shows the kinetic energy and incidence angle of the particles upon collision with the pipe wall in Fig. 7(c). Regarding the EW positions, the direction of the particles at the bend inlet gradually becomes parallel to the gravity direction with the increase in BA and bend length. Accordingly, the particle collision occurs toward the middle of the elbow. Fig. 8(b) reveals that the particles are highly concentrated at the bend outlet at a BA of 45°. When the BA increases to 90°, the collision occurs in the bend section instead of the horizontal pipe. The maximum EW position is also subject to the combined effect of IV and PS.

For the maximum EW rates, at similar locations of maximum EW rate where the bend is connected to the outlet pipe, the maximum kinetic energy increases from 1.22×10^{-6} J for a BA of 45° to 1.27×10^{-6} J for a BA of 60°. Moreover, the minimum incidence angle decreases from 77.9° to 76.8°, which means that the maximum EW rate is greater for a BA of 60°. As the maximum EW shifts toward the center of the bend with the BA increasing from 60° to 90°, the vertical height of the pipe inlet from the position of maximum kinetic energy and the kinetic energy of the particles under gravity decrease, which is evident from the corresponding kinetic energy in Fig. 8(a). The incidence angle remains almost un-
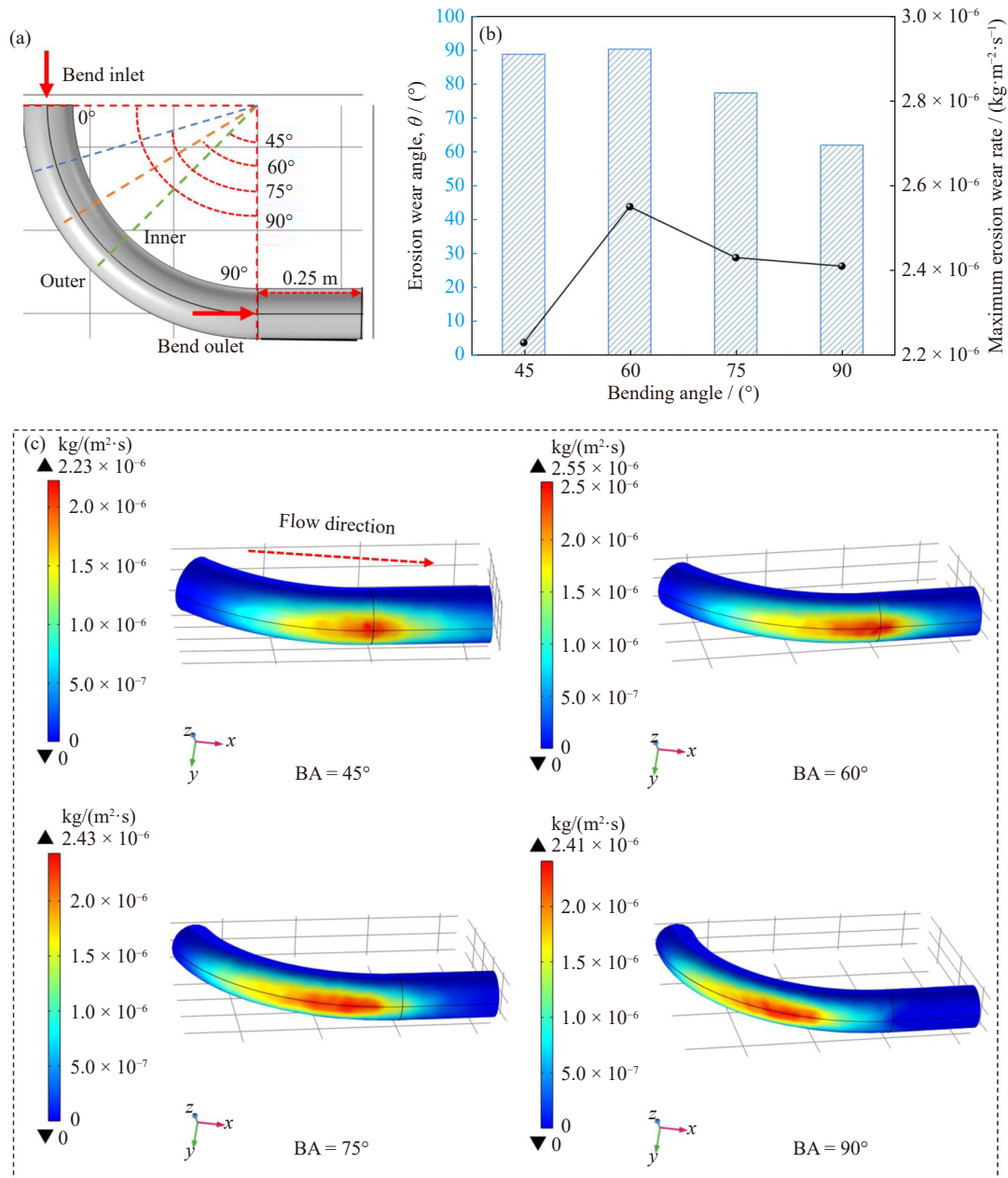
Fig. 7. Slurry transport at the bend with different bend angles (particle size of 650 μm and inlet velocity of 2.5 m/s): (a) intercepted geometric pipe, (b) maximum erosion wear rate and corresponding position, and (c) distribution of bend erosion wear rate at the bend.

changed, so the maximum EW rate decreases gradually from 60° to 90° BA.

4. Multiple factor coupling impact and sensitivity analysis

Considering the limitations of analyzing the effects of individual factors only, this work further discussed the differences caused by EW of bends under the combined effect of multiple factors. Fig. 9 shows the maximum EW rate of the bend for the combination of IV, PS, and BA. The maximum EW rate increases exponentially with IV and PS but not significantly with the increasing BA. This indicates that IV and PS have a synergistic effect on the EW of bends, and an in-

crease in both parameters exacerbates the damage. At high IVs, large particles in the slurry can maintain their original motion state, resulting in great particle kinetic energy and incidence angles and, consequently, severe EW at the bend location. In particular, the maximum EW rate is 5.68×10^{-6} kg·m^{-2}·s^{-1} for IV of 3.0 m·s^{-1}, PS of 650 μm, and BA of 60°. Fig. 10 shows the location of the maximum EW rate of the bend for the combination of the three factors. The maximum EW location is mainly at the outlet of the bend (close to 90°) as the BA increases for PS below or equal to 450 μm. However, the maximum EW location is closer to the center of the bend as the BA increases for PS above 450 μm. Given that the inertia force is low at low IV and small PS, the particles are less able to break through the fluid confinement,
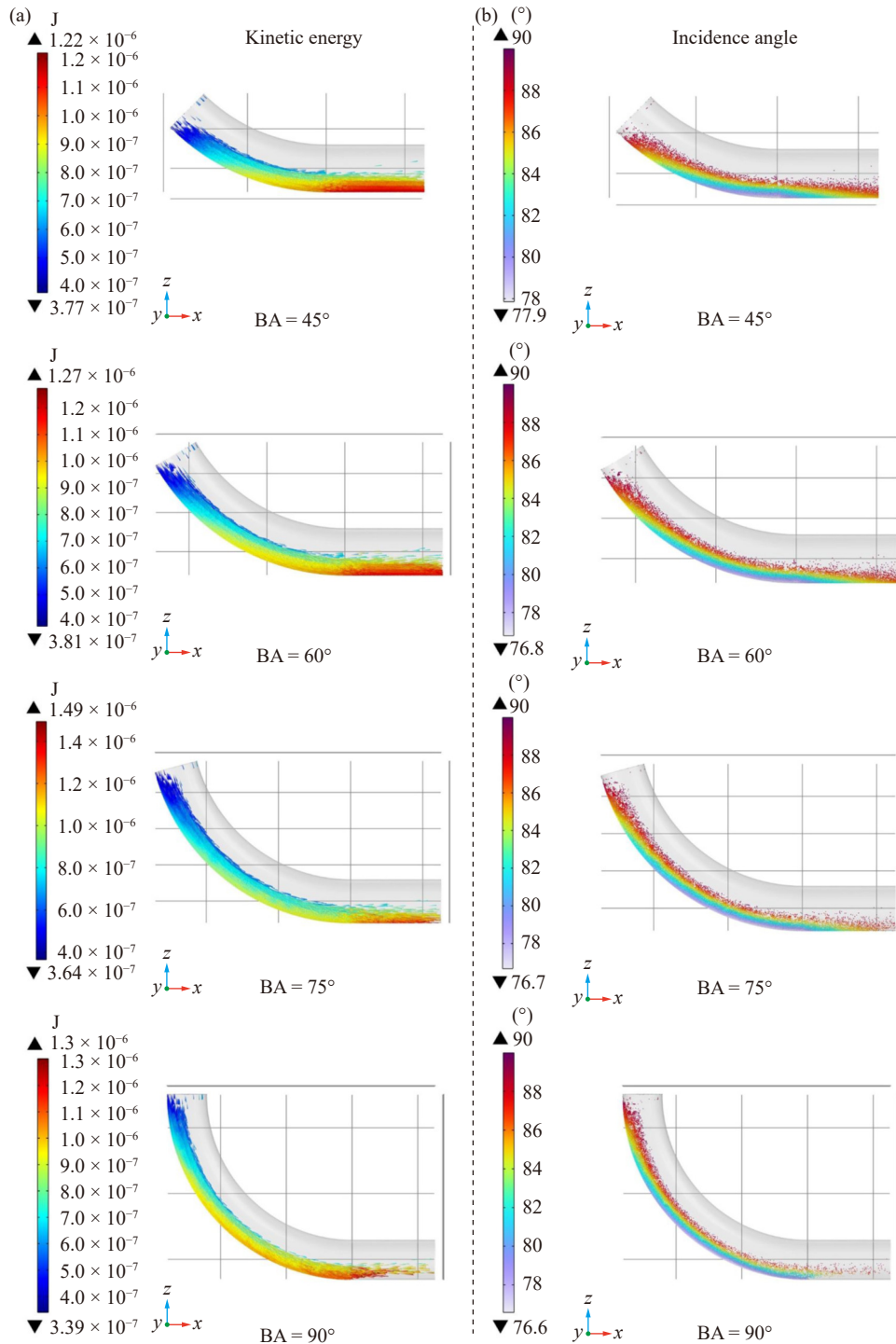
Fig. 8. Slurry transport at the bend with different bend angles (particle size of 650 μm and inlet velocity of 2.5 m/s): (a) particle kinetic energy and (b) particle incidence angle.

which is displaced farther by the fluid traction. Owing to centrifugal force, the particles collide frequently near the bend outlet at different BAs. By contrast, the particles are able to maintain inertial motion at high IVs and large PSs. With the increase in the BA, the particles collide near the bend center, which shifts toward the inlet, causing the position of maximum EW to move toward the inlet.

Sensitivity analysis of the influencing factors can provide an accurate understanding of the bend EW. Sixteen samples were selected for orthogonal analysis from the 64 sets of sim-

ulation results in Fig. 9 (see Supplementary Table S2 for details), and the importance of IV, PS, and BA was briefly compared by calculating the range [45–46]. Fig. 11(a) shows the range values of 1.77×10^{-6}, 2.14×10^{-6}, and 1.15×10^{-6} for IV, PS, and BA at the maximum EW rate, respectively. The order is PS > IV > BA because the higher the range, the greater the sensitivity. In addition, a relationship between the maximum EW rate and the three variables (IV, PS, and BA) was fitted to the data in Fig. 9, as shown in Eq. (13). A fitted correlation coefficient of 0.97 is obtained, indicating a good
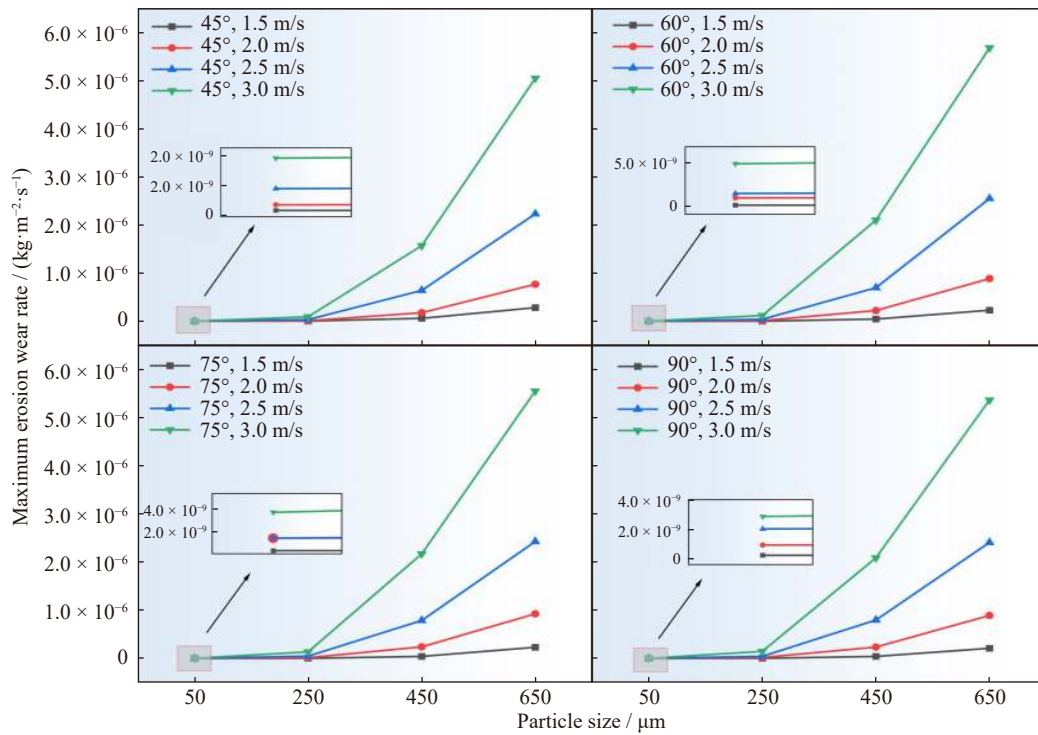
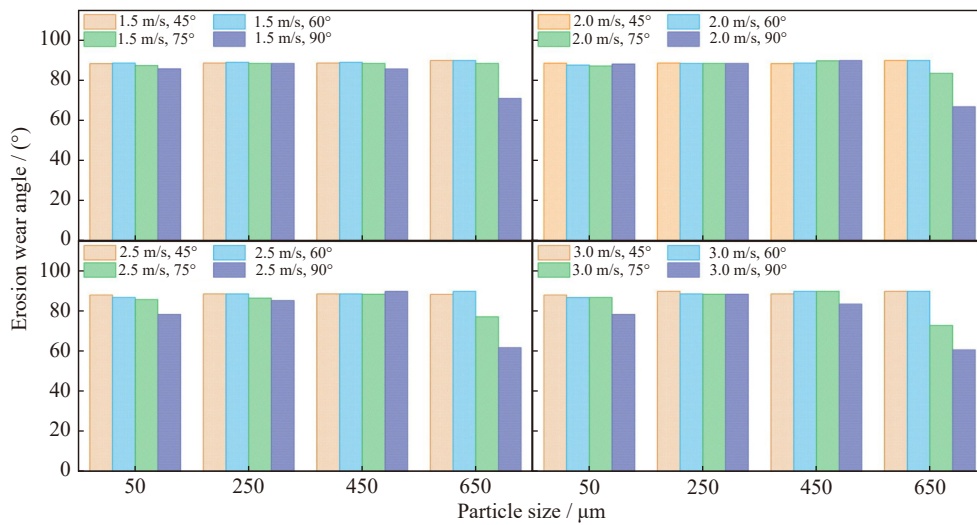Fig. 9.   Maximum erosion wear rate at the bend for different factors.

Fig. 10.   Location of maximum erosion wear at the bend for different factors.
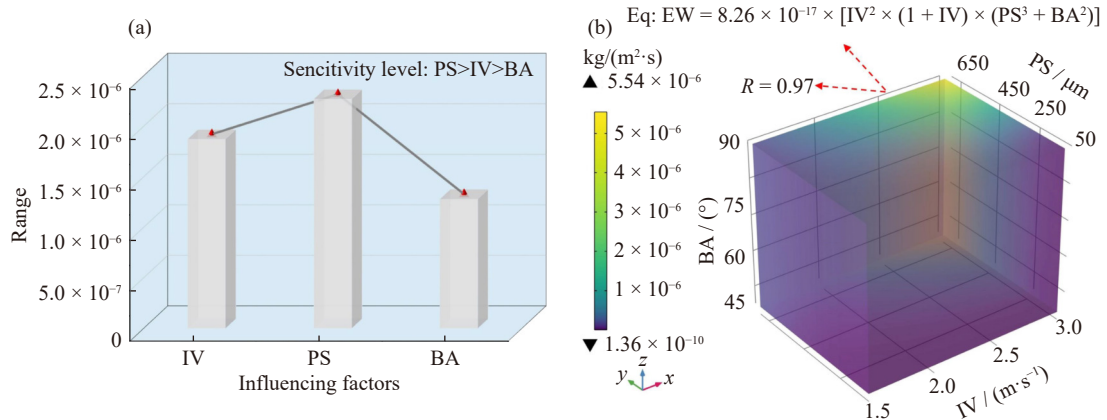

Fig. 11.   (a) Sensitivity level and (b) fitted function image.

fit. The function image is shown in Fig. 11(b).

$$EW = 8.26 \times 10^{-17} \times [IV^2 \times (1 + IV) \times (PS^3 + BA^2)] \quad (13)$$

On the basis of the above analysis, the outer wall of the bend should be thicker than the inner wall in the design of the pipeline, especially the outlet connection part of the bend should be reinforced to ensure the safety and stability of the pipeline transport system. Instead of IV and BA, using a small PS is highly effective in reducing the bend EW during actual slurry transport.

5. Conclusions

In this work, the numerical model is used to simulate slurry transportation in the pipe, focusing on the effects of the coupling of three factors, IV, PS, and BA, on the EW at the bend and analyzing them in detail in terms of particle kinetic energy and incidence angle. The major findings of this study are summarized as follows.

(1) Within the set parameter ranges, the EW rate of the slurry at the bend increases exponentially with IV and PS and first increases and then decreases with the increase in BA with the inflection point at 60°. At IV of 3.0 m·s^{-1}, PS of 650 μm, and BA of 60°, the bend EW was the most severe, and the maximum EW rate was 5.68×10^{-6} kg·m^{-2}·s^{-1}.

(2) Comprehensive analysis of the interaction among the three factors shows that an increase in IV and PS aggravates EW at the bend. The sensitivity levels of the three factors to the maximum EW rate are in the order PS > IV > BA. When PS is below or equal to 450 μm, the maximum EW position is mainly at the outlet of the bend. When PS is greater than 450 μm, the maximum EW position shifts toward the center of the bend with the increase in BA.

(3) A relationship between the maximum EW rate and the three variables is established with a correlation coefficient of 0.97. In practice, EW can be reduced by lowering the IV as much as possible, using small particles, and protecting the area around the bend outlet.

In this work, the effect of chemical corrosion on pipe wear was not considered. In some highly acidic slurries, chemical corrosion and EW can exhibit a degree of synergistic effect. In addition, bent pipes are susceptible to stress corrosion under high pressure conditions. The pipe diameter, pipe material, and the shape of the particles can also influence the degree of pipe wear. Further research on these phenomena is necessary.

Acknowledgements

Conflict of Interest

Qiusong Chen is an editorial board member and Yikai Liu is a youth editorial board member for this journal; they were not involved in the editorial review or the decision to publish this article. All authors declare that there are no competing interests.

Supplementary Information

The online version contains supplementary material available at https://doi.org/10.1007/s12613-023-2672-z.

References

[1] Q.M. Nguyen, J. Abouezzi, and L. Ristroph, Early turbulence and pulsatile flows enhance diodicity of Tesla's macrofluidic valve, *Nat. Commun.*, 12(2021), No. 1, art. No. 2884.

[2] R. Tarodiya and B.K. Gandhi, Hydraulic performance and erosive wear of centrifugal slurry pumps - A review, *Powder Technol.*, 305(2017), p. 27.

[3] Q.S. Chen, S.Y. Sun, Y.M. Wang, Q.L. Zhang, L.M. Zhu, and Y.K. Liu, *In-situ* remediation of phosphogypsum in a cement-free pathway: Utilization of ground granulated blast furnace slag and NaOH pretreatment, *Chemosphere*, 313(2023), art. No. 137412.

[4] M.E. Ibrahim and M. Medraj, Prediction and experimental evaluation of the threshold velocity in water droplet erosion, *Mater. Des.*, 213(2022), art. No. 110312.

[5] I. Marusic, D. Chandran, A. Rouhi, *et al.*, An energy-efficient pathway to turbulent drag reduction, *Nat. Commun.*, 12(2021), art. No. 5805.

[6] G. Singh, S. Kumar, and S.K. Mohapatra, Erosion wear in a slurry pipe with multisized coal and bottom-ash slurries, *Mater. Today*, 4(2017), No. 2, p. 3565.

[7] A.X. Wu, Z. Ruan, and J.D. Wang, Rheological behavior of paste in metal mines, *Int. J. Miner. Metall. Mater.*, 29(2022), No. 4, p. 717.

[8] D.L. Wang, Q.L. Zhang, Q.S. Chen, C.C. Qi, Y. Feng, and C.C. Xiao, Temperature variation characteristics in flocculation settlement of tailings and its mechanism, *Int. J. Miner. Metall. Mater.*, 27(2020), No. 11, p. 1438.

[9] A. Uzi, Y. Ben Ami, and A. Levy, Erosion prediction of industrial conveying pipelines, *Powder Technol.*, 309(2017), p. 49.

[10] H.Z. Jiao, W.B. Yang, Z.E. Ruan, J.X. Yu, J.H. Liu, and Y.X. Yang, Microscale mechanism of tailing thickening in metal mines, *Int. J. Miner. Metall. Mater.*, 30(2023), No. 8, p. 1538.

[11] Q.S. Chen, L.M. Zhu, Y.M. Wang, J. Chen, and C.C. Qi, The carbon uptake and mechanical property of cemented paste backfill carbonation curing for low concentration of CO$_2$, *Sci. Total Environ.*, 852(2022), art. No. 158516.

[12] R.K. Rathore, P.K. Gupta, and N. Kumar, Numerical investigation of zinc tailings slurry flow field in a horizontal pipeline, *Mater. Today Proc.*, 45(2021), p. 2702.

[13] A. Uzi and A. Levy, Energy absorption by the particle and the surface during impact, *Wear*, 404-405(2018), p. 92.

[14] R. Camassa, D.M. Harris, R. Hunt, Z. Kilic, and R.M. McLaughlin, A first-principle mechanism for particulate aggregation and self-assembly in stratified fluids, *Nat. Commun.*, 10(2019), No. 1, art. No. 5804.

[15] Q.L. Zhang, Y.T. Li, Q.S. Chen, Y.K. Liu, Y. Feng, and D.L. Wang, Effects of temperatures and pH values on rheological properties of cemented paste backfill, *J. Cent. South Univ.*, 28(2021), No. 6, p. 1707.

[16] S. Dhodapkar, P. Solt, and G. Klinzing, Understanding bends in pneumatic conveying systems, *Chem. Eng.*, 116(2009), p. 53.

[17] S.S. Rajahram, T.J. Harvey, and R.J.K. Wood, Erosion–corrosion resistance of engineering materials in various test condi-

1620

Int. J. Miner. Metall. Mater., Vol. 30, No. 8, Aug. 2023

tions, *Wear*, 267(2009), No. 1-4, p. 244.

[18] Y.F. Liu, Y.L. Zhao, and J. Yao, Synergistic erosion-corrosion behavior of X80 pipeline steel at various impingement angles in two-phase flow impingement, *Wear*, 466-467(2021), art. No. 203572.

[19] H. Zhou, Q.F. Ji, W. Liu, H.Y. Ma, Y. Lei, and K.Q. Zhu, Experimental study on erosion-corrosion behavior of liquid–solid swirling flow in pipeline, *Mater. Des.*, 214(2022), art. No. 110376.

[20] J.H. Wang, T.F. Zhang, and S.G. Wang, Heterogeneous ice slurry flow and concentration distribution in horizontal pipes, *Int. J. Heat Fluid Flow*, 44(2013), p. 425.

[21] H. Zhang, Y.Q. Tan, D.M. Yang, *et al.*, Numerical investigation of the location of maximum erosive wear damage in elbow: Effect of slurry velocity, bend orientation and angle of elbow, *Powder Technol.*, 217(2012), p. 467.

[22] Y.Q. Tan, H. Zhang, D.M. Yang, S.Q. Jiang, J.H. Song, and Y. Sheng, Numerical simulation of concrete pumping process and investigation of wear mechanism of the piping wall, *Tribol. Int.*, 46(2012), No. 1, p. 137.

[23] B.Q. Wu, X.D. Wang, X.X. Liu, G.G. Xu, and S.B. Zhu, Numerical simulation of erosion and fatigue failure the coal gangue paste filling caused to pumping pipes, *Eng. Fail. Anal.*, 134(2022), art. No. 106081.

[24] V. Kannojiya, M. Deshwal, and D. Deshwal, Numerical analysis of solid particle erosion in pipe elbow, *Mater. Today Proc.*, 5(2018), No. 2, p. 5021.

[25] Q.C. Wang, Q.Y. Huang, N.R. Wang, *et al.*, An experimental and numerical study of slurry erosion behavior in a horizontal elbow and elbows in series, *Eng. Fail. Anal.*, 130(2021), art. No. 105779.

[26] M.M. Zhou, S.B. Kuang, F. Xiao, K. Luo, and A.B. Yu, CFD-DEM analysis of hydraulic conveying bends: Interaction between pipe orientation and flow regime, *Powder Technol.*, 392(2021), p. 619.

[27] M. Parsi, M. Agrawal, V. Srinivasan, *et al.*, CFD simulation of sand particle erosion in gas-dominant multiphase flow, *J. Nat. Gas Sci. Eng.*, 27(2015), p. 706.

[28] J.X. Zhang, J.A. Kang, J.C. Fan, and J.C. Gao, Study on erosion wear of fracturing pipeline under the action of multiphase flow in oil & gas industry, *J. Nat. Gas Sci. Eng.*, 32(2016), p. 334.

[29] M. Parsi, R.E. Vieira, N. Kesana, B.S. McLaury, and S.A. Shirazi, Ultrasonic measurements of sand particle erosion in gas dominant multiphase churn flow in vertical pipes, *Wear*, 328-329(2015), p. 401.

[30] S.N. Shah and S. Jain, Coiled tubing erosion during hydraulic fracturing slurry flow, *Wear*, 264(2008), No. 3-4, p. 279.

[31] N. Lin, H.Q. Lan, Y.G. Xu, S.H. Dong, and G. Barber, Effect of the gas-solid two-phase flow velocity on elbow erosion, *J. Nat. Gas Sci. Eng.*, 26(2015), p. 581.

[32] Q.B. Nguyen, V.B. Nguyen, C.Y.H. Lim, *et al.*, Effect of impact angle and testing time on erosion of stainless steel at high-

er velocities, *Wear*, 321(2014), p. 87.

[33] J.K. Chen, Y.S. Wang, X.F. Li, R.Y. He, S. Han, and Y.L. Chen, Erosion prediction of liquid-particle two-phase flow in pipeline elbows via CFD–DEM coupling method, *Powder Technol.*, 275(2015), p. 182.

[34] M. Tiberga, A. Hennink, J.L. Kloosterman, and D. Lathouwers, A high-order discontinuous Galerkin solver for the incompressible RANS equations coupled to the $k-\epsilon$, *Comput. Fluids*, 212(2020), art. No. 104710.

[35] B.E. Launder and B.I. Sharma, Application of the energy-dissipation model of turbulence to the calculation of flow near a spinning disc, *Lett. Heat Mass Transf.*, 1(1974), No. 2, p. 131.

[36] Y. Sun, M.L. Liu, Y. Xiao, and Y.F. Chen, A novel molecular communication inspired detection method for the evolution of atherosclerosis, *Comput. Meth. Programs Biomed.*, 219(2022), art. No. 106756.

[37] M. Rafiee, M.J.H. Simmons, A. Ingram, and E.H. Stitt, Development of positron emission particle tracking for studying laminar mixing in Kenics static mixer, *Chem. Eng. Res. Des.*, 91(2013), No. 11, p. 2106.

[38] A. Mansouri, *Development of Erosion Equations for Slurry Flows*, Advis. Board Rep. Erosion/Corrosion Res. Center, Univ. Tulsa, Tulsa, 2015, p. 48.

[39] L. Zeng, G.A. Zhang, and X.P. Guo, Erosion-corrosion at different locations of X65 carbon steel elbow, *Corros. Sci.*, 85(2014), p. 318.

[40] M.H. Zolfagharnasab, M. Salimi, H. Zolfagharnasab, H. Alimoradi, M. Shams, and C. Aghanajafi, A novel numerical investigation of erosion wear over various 90-degree elbow duct sections, *Powder Technol.*, 380(2021), p. 1.

[41] M.A. Al-Bukhaiti, S.M. Ahmed, F.M.F. Badran, and K.M. Emara, Effect of impingement angle on slurry erosion behaviour and mechanisms of 1017 steel and high-chromium white cast iron, *Wear*, 262(2007), No. 9-10, p. 1187.

[42] R.E. Vieira, A. Mansouri, B.S. McLaury, and S.A. Shirazi, Experimental and computational study of erosion in elbows due to sand particles in air flow, *Powder Technol.*, 288(2016), p. 339.

[43] X.H. Chen, B.S. McLaury, and S.A. Shirazi, Numerical and experimental investigation of the relative erosion severity between plugged Tees and elbows in dilute gas/solid two-phase flow, *Wear*, 261(2006), No. 7-8, p. 715.

[44] D.J. Blanchard, P. Griffith, and E. Rabinowicz, Erosion of a pipe bend by solid particles entrained in water, *J. Manuf. Sci. Eng.*, 106(1984), No. 3, p. 213.

[45] P.C. Kang, Q.Q. Zhao, S.Q. Guo, *et al.*, Optimisation of the spark plasma sintering process for high volume fraction SiCp/Al composites by orthogonal experimental design, *Ceram. Int.*, 47(2021), No. 3, p. 3816.

[46] Q. Li, Z.Y. Peng, W.B. Jiang, *et al.*, Optimization of Ti−Zr−Cr−Fe alloys for 45 MPa metal hydride hydrogen compressors using orthogonal analysis, *J. Alloys Compd.*, 889(2021), art. No. 161629.